

HQ-50K: A Large-scale, High-quality Dataset for Image Restoration

Qinhong Yang¹ Dongdong Chen² Zhentao Tan¹ Qiankun Liu¹ Qi Chu¹
 Jianmin Bao² Lu Yuan² Gang Hua³, Nenghai Yu¹

¹University of Science and Technology of China ²Microsoft ³Xi'an Jiaotong University

{qhyang233@mail., tzt@mail., liuqk3@mail., qchu@, ynh@}ustc.edu.cn

{jianbao, luyuan}@microsoft.com, {cddlyf, ganghua}@gmail.com

Abstract

This paper introduces a new large-scale image restoration dataset, called **HQ-50K**, which contains 50,000 high-quality images with rich texture details and semantic diversity. We analyze existing image restoration datasets from five different perspectives, including data scale, resolution, compression rates, texture details, and semantic coverage. However, we find that all of these datasets are deficient in some aspects. In contrast, HQ-50K considers all of these five aspects during the data curation process and meets all requirements. We also present a new Degradation-Aware Mixture of Expert (DAMoE) model, which enables a single model to handle multiple corruption types and unknown levels. Our extensive experiments demonstrate that HQ-50K consistently improves the performance on various image restoration tasks, such as super-resolution, denoising, dejpeg, and deraining. Furthermore, our proposed DAMoE, trained on our HQ-50K, outperforms existing state-of-the-art unified models designed for multiple restoration tasks and levels. The dataset and code are available at <https://github.com/littleYaang/HQ-50K>.

1. Introduction

Large-scale high-quality datasets play an essential role in the deep learning era, which act as the catalyst stimulating and accelerating of technique development. In the image understanding field, there are many large-scale datasets proposed in the past years, *e.g.*, ImageNet [21] and COCO [33], making great contribution to the field. And the data scale is still continuing growing up. But for the low-level image restoration field, even though some datasets have been collected for specific restoration tasks, *e.g.*, super-resolution (SR) [2, 32], denoising [4, 61] and deraining [52, 60], there is still no large-scale dataset dedicatedly developed. By analyzing existing restoration datasets from five aspects, *i.e.*, data scale, image resolution, compression rates, texture details and semantic coverage, we find that all existing restora-

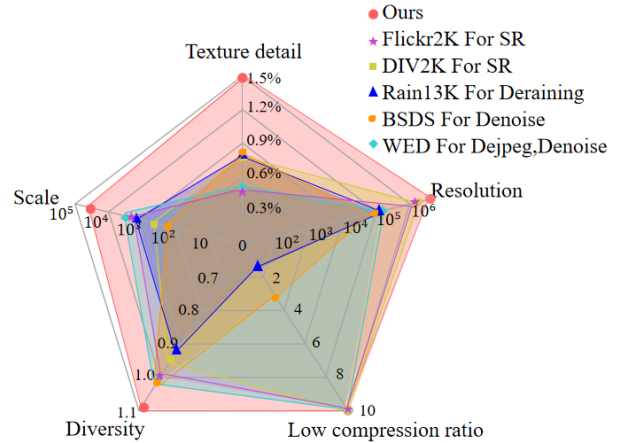


Figure 1. Comparison between our HQ-50K and existing restoration datasets from five aspects. Our dataset considers all five aspects simultaneously while existing datasets are always deficient in some aspects.

tion datasets are deficient in some aspects.

In this paper, we move a step forward and propose a large-scale, high-quality dataset HQ-50K for image restoration, which considers the above five aspects simultaneously.

- **Large-Scale.** Our HQ-50K contains 50,000 images, while the commonly used restoration dataset BSDS400 [4], DIV2K [2], Flickr2K [32], WED [35], and Rain13K [58] only contains 400, 800, 2650, 4744 and 1212 clean images respectively. Such a larger scale can help better exploit the full potentials of more advanced model architectures.
- **High-Resolution.** HQ-50K contains high-resolution images with an average of 2,509,509 pixels, making them superior in resolution compared to other existing datasets. By utilizing HQ-50K, restoration models can enhance their ability to learn more realistic textures, particularly for tasks that involve predicting high-resolution images, such as SR.

- *Compression Rates.* Many images on the internet use compression techniques like JPEG compression to save storage space. To ensure that the images we select have minimal compression distortion, we only choose those with low compression rates by measuring the bpp metric (*i.e.*, “bits per pixel”). Similar to resolution, this selection criteria is important to improve the performance of restoration tasks such as SR and Dejpeg.
- *Rich texture details.* In addition to compression, images on the internet also have an imbalanced frequency distribution, *i.e.*, a large portion of images lack rich texture details (*e.g.*, simple background). So indiscriminately scaling up data by crawling high-resolution images without selection will lead to an unbalanced dataset. Training the model on such data will result in poor performance when dealing with images that have intricate texture details. To overcome this, we perform frequency analysis and ensure that we select images from different frequency bands to achieve a balanced distribution when building HQ-50K .
- *Semantic Coverage.* Existing restoration datasets, such as DIV2K [2] and Flickr2K [32], primarily comprise outdoor natural images. We notice that models trained on these datasets do not perform as well for indoor or artificial images, such as maps, posters, and handwriting. To develop a more generalized restoration model, we collect images that cover a broader range of semantic categories in a more balanced way.

Following the common synthesis for learning pipeline, HQ-50K can be used to serve different restoration tasks by simulating the corresponding degradation process upon the clean images. Additionally, we also offer 1250 test images that span across various semantic categories and frequency ranges. This new benchmark can facilitate detailed and fine-grained performance comparison and analysis.

In addition to HQ-50K , we propose a new model called the Degradation-Aware Mixture of Expert (DAMoE), which enables a unified approach to handle various restoration tasks and unknown degradation levels. To our knowledge, this is the first attempt at integrating the Mixture of Expert (MoE) concept into the image restoration field. The DAMoE model shares all the modules and parameters for different tasks, except for the experts in the MoE layers. It dynamically adjusts the inference process of the network through expert mechanism to adapt to different restoration task. For the MoE layers, we introduce two types of MoE blocks, namely, Hard-MoE and Soft-MoE, and demonstrate that their combination yields the best overall performance. Our contributions can be summarized as two-folds:

- We propose a large-scale, high-quality dataset for image restoration tasks. Through extensive experiments,

we demonstrate that the proposed dataset can improve the restoration performance for different tasks.

- We present the first attempt at integrating MoE into the image restoration tasks and propose a new unified image restoration model “DAMoE”. It achieves better performance than existing unified restoration models.

2. Related Works

Image Restoration Datasets. For low-level image processing tasks, it is often very difficult and expensive to collect paired images from the real world to build a dataset. Additionally, these datasets may be limited to a small number of captured scenes and devices, making it challenging to apply the results to other situations. Therefore, it is common to synthesize degraded images from clean images as a strategy. Most existing image restoration datasets are designed for specific degradation types, such as DIV2K [2] and Flickr2K [32], which are commonly used for SR tasks and include 800 and 2,650 high-resolution images, respectively. For denoising and dejpeg tasks, there are 400 images in the BSDS dataset [4] and 4,744 images in Waterloo Exploration Database (WED) dataset [35]. Some color denoising models are trained on the polyU Real World Noisy Images Dataset [51] and Smartphone Image Denoising Dataset (SIDD) [1]. For deraining tasks, Rain100L/Rain100H [52], Rain800 [60], Rain1200 [59], Rain1400 [23] and Rain13K [58] are widely used. However, nearly all of these datasets have a limited scale, making it difficult to train large-scale models. ImageNet [21], which consists of about 1.3 million images, is recently used for image restoration pre-training [7, 29], but it still suffers from low resolution and high compression ratios. Recently, the large-scale Laion-5B [41] dataset was released for multimodal pretraining, and one intuitive way to create a large-scale restoration dataset is to use the high-resolution subset of Laion-5B, called “Laion-HR” . However, most images in Laion-HR lack rich texture details, which are essential for low-level image restoration tasks. In the following section, we will provide a detailed analysis of existing datasets from five aspects and show that our dataset is the first to meet all the requirements.

Image Restoration Methods. In recent years, the rapid development of deep learning has led to impressive performance in data-driven methods for image restoration tasks, such as denoising [3, 55, 5], super-resolution [63, 11, 37], dejpeg [28, 54], and deraining [6, 22, 39]. At an early stage, CNN-based methods were trained for a specific degradation type with a fixed degradation level. Taking SR as an example, deep learning based methods [12, 44, 24, 25, 63, 11, 37] achieved amazing results, but the model was designed solely for the SR task and could only handle a specific down-sampling scale. This poor generalization and

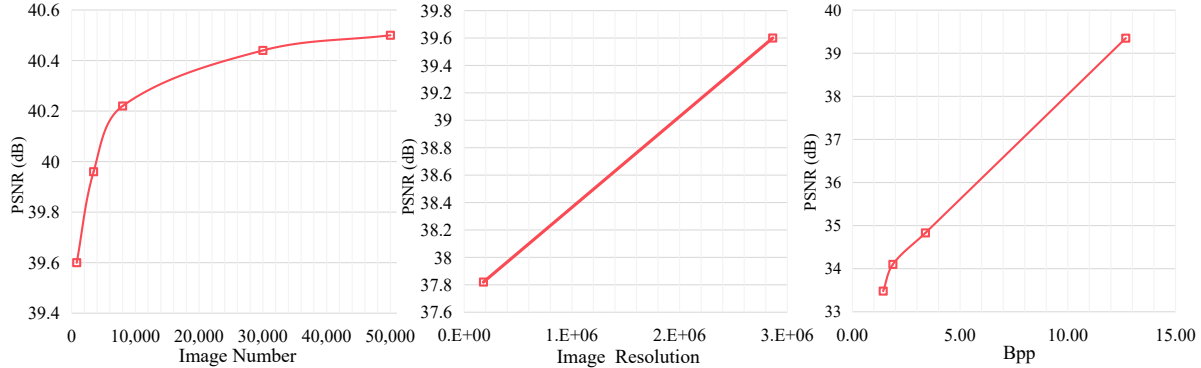


Figure 2. Study on different aspects of dataset on model performance ((a) image number, (b) image resolution , (c) Bpp). Results are tested on Manga109 [17] for image SR ($\times 2$).

limited applicability to other tasks also existed in deraining [6, 16, 18, 49] and denoising [61, 62, 5]. Recently, more methods have shown impressive performance on various image restoration tasks. Among them, transformer-based methods [7, 29, 48, 56, 31] are usually superior to CNN-based methods [8, 9, 46, 57], thanks to their strong ability to learn long-range dependencies between image patch sequences. While these models are suitable for multiple tasks, they still need to be trained separately for each specific task and degradation level in order to achieve good performance.

Recently, some latest research has been proposed to study unified image restoration, aiming to restore images under various degradation in a single network. For instance, AirNet [27] proposed to extract specific degradation types through a learned encoder, and GIQE [45] randomly combined various degradation types during training. To tackle multiple types of adverse weathers, Chen *et al.* [10] proposed a unified model with two-stage knowledge learning and TransWeather [47] proposed a transformer-based end-to-end model. In this paper, inspired by the MoE idea, we propose a MoE-based unified image restoration model that can handle different low-level tasks including SR, denoising, dejpeg and derain. Although MoE models have been extensively studied in scaling up both vision [40, 50] and text models [26, 42, 13], to the best of our knowledge, this is the first attempt at applying MoE to low-level vision tasks.

3. HQ-50K Dataset

In this section, before introducing our HQ-50K, we first present a comprehensive analysis of the existing restoration datasets based on the five aforementioned aspects.

Large-Scale. Large-scale datasets have been proven to be crucial for achieving good results in deep learning for image understanding, particularly for training large models. In order to demonstrate the significance of data scale in the image restoration field, we trained SwinIR [31] on different subsets of our HQ-50K (which will be described later), each

with a different number of training images but the same attributes across four other aspects. As shown in the left of Figure 2, the performance of SwinIR improves as the number of training images increases, showing that larger-scale dataset also plays an essential role in image restoration field. Nevertheless, existing restoration datasets that have been specifically collected remain severely limited in scale.

High Resolution. Despite some existing restoration works [7, 29] utilizing ImageNet [21] for large-scale pretraining, they still require further fine-tuning on specific high-quality restoration datasets. This is partially due to the fact that most images in ImageNet have low resolution and quality. In order to systematically explore the impact of resolution, we resize the images from DIV2K [2] to the same resolution as the average pixel count of images in ImageNet (200,000 pixels). As depicted in the middle section of Figure 2, decreasing the image resolution significantly impairs the performance of SR.

Low Compression Rate. The majority of images in existing restoration datasets are sourced from the internet, and many of them have been compressed using image compression techniques to reduce storage requirements. However, high compression rates can lead to significant information loss and distortion artifacts. Since the goal of image restoration is often to generate high-quality images, training models on highly compressed images will result in poor performance. To quantitatively assess the impact of compression ratios on performance, we trained SwinIR on the DIV2K dataset using different levels of compression, as measured in bits per pixel (bpp). A higher bpp value indicates a lower degree of compression for an image. As illustrated on the right-hand side of Figure 2, lower compression ratios enable the model to achieve better performance.

Rich Texture Details. Similar to compression rates, the richness of image texture details in a dataset would also significantly impact model performance. Take the high-resolution subset of Laion-5B [41] (referred to as “Laion-

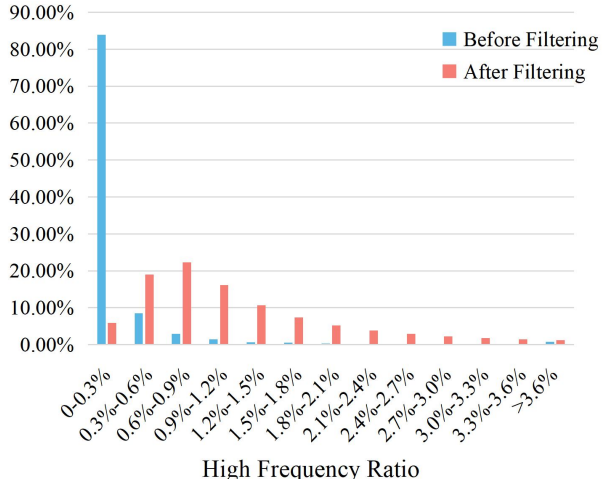


Figure 3. The frequency distribution of the original Laion-HR (blue histogram) and our HQ-50K (orange histogram).

Table 1. Results on different frequency bands of Urban100 [19]

	Urban100	Low-freq. Subset	High-freq. Subset
High-freq Ratio	1.514%	0.2035%	15.84%
DIV2K	33.34/0.9391	37.99/0.9625	32.29/0.9359
Laion-HR	32.64/0.9324	37.43/0.9586	31.43/0.9280

HR”) as a counter-example, although the images in this subset have high resolutions and a large data scale, its texture information details are seriously insufficient to train a good restoration model. As shown in Figure 3, frequency analysis¹ performed on Laion-HR shows that over 80% of the images in this subset lack sufficient high-frequency information. This makes the model trained on Laion-HR incapable of handling images with complex texture structures that contain high-frequency information, such as animal fur, leaves or branches, dense windows in buildings, and other fine-scale regular structures. To validate this, we trained SwinIR on both DIV2K and Laion-HR and compared their performance on Urban100 [19], as shown in Table 1. The model trained on Laion-HR performs considerably worse than the model trained on DIV2K. We further divide Urban100 into two subsets: high-frequency images and low-frequency images, and find that larger performance gap exists in high-frequency images.

Semantic Coverage. To train a generalizable model that performs well on images of different semantic categories, in our work, we categorize images into three broad classes: outdoor, indoor, and artificial. The outdoor class contains images captured in nature and architecture, people, animals, and transportation. The indoor class includes images of indoor scenes, furniture, food, and objects. The artificial class contains images that have been post-processed or synthe-

¹Here we map the image into the frequency domain with DFT transformation, then calculate the ratio of high-frequency component (i.e., High-frequency ratio) in the whole image.

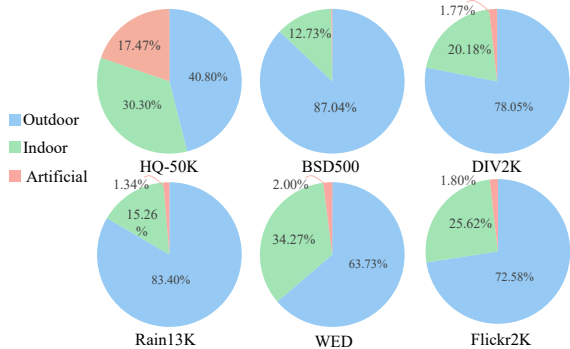


Figure 4. Semantic distribution of existing datasets in three broad categories: outdoor, indoor, artificial.

sized directly, such as posters, maps, texts, and comics. To measure the diversity of category distribution in a dataset, we calculate the entropy of semantic category using the formula: $H = -\sum_{i=1}^n p_i \log p_i$ where p_i is the percentage of the i -th class in the total dataset. The larger the value of H , the more evenly distributed the dataset is across all the semantic categories we define.

Our analysis of existing image restoration datasets revealed that they often have an unbalanced semantic distribution (shown in Figure 4), with a large portion of images belonging to the outdoor class, while indoor and artificial images are relatively fewer (especially artificial images). Our experiments (Table 4 and supplementary material) demonstrate that training a model on such an unbalanced dataset results in suboptimal performance on categories with limited coverage.

3.1. Dataset Collection and Processing of HQ-50K

To ensure the high quality of the proposed dataset, we have taken into account the aforementioned five aspects during the construction process. First, we collect a large number of images from the Internet and existing large-scale dataset [41]. To ensure *balanced semantic coverage*, we select images from the above three broad categories, each of which contains several sub-categories. Since we do not have the semantic label for the collected images, we instead leverage the pretrained CLIP [38] to categorize each image. Moreover, we try to balance the image number of each category and guarantee that each category would have a sufficient number of images. The final semantic distribution can be seen in Figure 4.

Next, we apply a series of filtering strategies to carefully remove images that did not meet the requirements. Specifically, to fulfill the *high resolution* requirement, we discard images with a length or width smaller than 1024 pixels. The final average pixel number is 2,509,509. To meet the *low compression ratio* requirement, we filter out the images that occupy less than 500KB storage space, resulting

Table 2. Statistical comparison of different datasets across five aspects: Scale, Resolution (Avg.pixels), Compression rates(bpp), Texture details (High-frequency ratio), and Semantic Coverage (Diversity).

Dataset	Task	Scale \uparrow	Avg.pixels \uparrow	bpp \uparrow	High-frequency Ratio \uparrow	Diversity \uparrow
DIV2K [2]	SR	800	2,788,027	12.69	0.8227%	0.997
Flickr2K [32]	SR	2,650	2,763,878	12.76	0.5369%	1.032
BSDS400 [4]	Denoising	400	154,401	3.77	0.8863%	1.092
WED [35]	Denoising, Dejpeg	4,744	218,576	24.74	0.5818%	1.068
Rain13K [58]	Derain	1,212	209,256	1.5357	1.0858%	0.934
ImageNet	High-level Tasks	1,281,167	219,175	4.72	1.0930%	1.036
Laion-HR	Multimodal Pretraining	170,000,000	3,117,066	1.57	0.1918%	1.099
HQ-50K (Ours)	Low-level Tasks	50,000	2,509,509	12.86	1.4270%	1.143

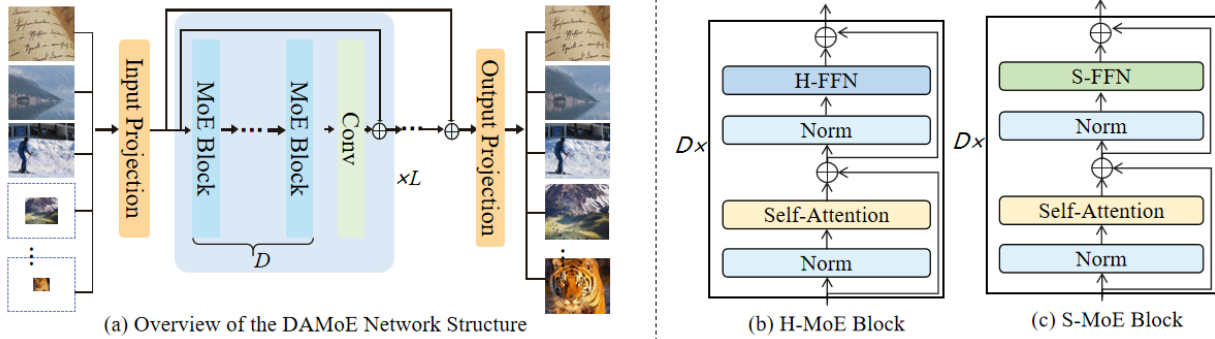


Figure 5. Illustration of the structure of Degradation-Aware Mixture of Expert (DAMoE). \oplus : element-wise addition. (a) Overview of DAMoE; (b) H-MoE Block introduces H-MoE layer while (c) S-MoE Block introduces S-MoE layer.

in a final average bpp of HQ-50K at 12.86. For the *texture detail* requirement, we calculate the high-frequency ratio of each image and removed images with a high-frequency ratio of less than 0.5%. We also ensure that the distribution of high-frequency ratio was wide enough to approach a normal distribution, thereby improving the generalization of each frequency domain interval. After filtering, the final frequency distribution is displayed in Figure 3 (orange histogram). Ultimately, 50,000 high-quality images, which is approximately 5.6% of all collected images, are selected and denoted as HQ-50K.

In addition to the 50,000 training images, we further collect 1250 test images that spanned across each semantic sub-category to help analyze the performance in a fine-grained manner.

3.2. Data Statistics of HQ-50K

Table 2 presents the detailed statistics of our HQ-50K and existing image restoration datasets. To summarize, HQ-50K is superior to existing datasets in terms of:

Number of images. To the best of our knowledge, HQ-50K has the largest scale compared with other datasets that are dedicated for image restoration tasks. It contains 50K images, which is $60\times$ larger than DIV2K[2].

High resolution. The average pixel number of each image in HQ-50K is comparable to DIV2K[2] and Flickr2K[32], but much larger than BSDS400[4], WED[35], Rain13K and

ImageNet[21].

Low compression ratio. HQ-50K is carefully filtered as stated in Section 3.1. It takes the second place in terms of bpp, which is only inferior WED [35]. However, HQ-50K has $10\times$ more images than WED [35]

Rich texture Details. The proposed HQ-50K has the best texture detail richness as measured by high-frequency ratio. Compared to Laion-HR, it also has a more balanced frequency distribution as shown in Figure 3.

Semantic diversity. HQ-50K also show the best semantic coverage and most balanced semantic distribution as shown in Figure 4. We have visualized the example images for each semantic sub-category in the supplementary material.

4. DAMoE for Unified Image Restoration

Our DAMoE is designed to handle a wide range of restoration tasks (*e.g.*, denoising, SR, deraining and dejpeg) and degradation levels (*e.g.*, $\times 2, \times 3, \times 4$ settings in SR) through a unified single model. As illustrated in Figure 5 (a), DAMoE employs shared modules and parameters for different tasks with different levels of degradation, except for the experts in MoE layers, which are dedicated to specific tasks (H-MoE) or dynamically activated based on input (S-MoE). Specifically, let $H \times W$ denote the input resolution of DAMoE. For tasks with lower resolution inputs (*e.g.*, SR), we standardize the input resolution by up-

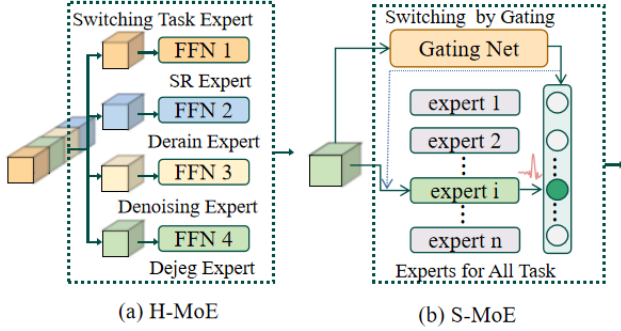


Figure 6. (a) H-MoE layer applies task-specific experts to different tasks. For one task, different levels of degradation share the same expert. (b) S-MoE layer processes multi-task input by a gating network, which means that all experts are visible to all tasks.

Table 3. Super resolution results on Set14 and Manga109 by using different training datasets.

scale	Training Set	Set14		Manga109	
		PSNR	SSIM	PSNR	SSIM
x2	DF2K	34.46	0.9250	39.92	0.9797
	HQ-50K	34.81	0.9262	40.50	0.9811
x3	DF2K	30.93	0.8534	35.12	0.9537
	HQ-50K	31.15	0.8542	35.21	0.9541
x4	DF2K	29.09	0.7950	32.03	0.9260
	HQ-50K	29.35	0.7953	32.36	0.9277

sampling the input to $H \times W$ with bicubic interpolation. Then, for an input image $I_{in} \in \mathbb{R}^{3 \times H \times W}$, a convolution-based projection layer is utilized to extract shallow features $X \in \mathbb{R}^{C \times H \times W}$ from I_{in} , where C represents the feature channel dimension. Before feeding X to several following transformer blocks, a learnable task embedding $e_i^{task} \in \mathbb{R}^{C \times 1 \times 1}$, $i = \{1, \dots, N\}$, where N indicates the number of tasks, is added to X . The backbone mainly comprises multiple MoE blocks and convolution layers. Thanks to the effective receptive fields of shifted windows [34] and self-attention, high-frequency texture and structural details of images can be effectively restored. We also use several skip-connections to combine shallow features with deep features. Finally, the output image $I_{out} \in \mathbb{R}^{3 \times H \times W}$ is reconstructed by a convolution-based projection layer.

4.1. Mixture of Expert Layer

Taking inspiration from the Mixture of Expert (MoE) mechanism [20, 42, 13], we incorporate MoE layers in our transformer backbone by substituting the feed forward network (FFN) layer with a MoE layer. The MoE layer comprises a collection of n experts E_1, E_2, \dots, E_n and a routing strategy. Given an input feature $x \in \mathbb{R}^C$, which represents a feature vector from a single spatial position of the feature maps, the MoE layer produces the output $y \in \mathbb{R}^C$, which is

Table 4. Super resolution results on our proposed fine-grained evaluation benchmark by using different training datasets.

scale	Training Set	Outdoor		Indoor		Artificial	
		PSNR	SSIM	PSNR	SSIM	PSNR	SSIM
x2	DIV2K	30.77	0.9008	31.21	0.9053	30.31	0.9120
	HQ-50K	31.00	0.9067	31.52	0.9134	30.46	0.9257
x3	DIV2K	27.54	0.8044	28.00	0.8201	26.64	0.8384
	HQ-50K	27.69	0.8086	28.20	0.8224	27.47	0.8504
x4	DIV2K	25.97	0.7334	26.40	0.7557	24.79	0.7799
	HQ-50K	26.18	0.7388	26.60	0.7614	25.81	0.7862

Table 5. Results comparison (“PSNR”) on the denoising task by using different training datasets.

TrainingSet	CBSD68[36]			Kodak24[15]		
	15	25	50	15	25	50
BSDS400+WED	34.29	31.66	28.43	35.25	32.82	29.79
HQ-50K	34.38	31.70	28.53	35.30	32.83	30.03

Table 6. Results comparison (“PSNR”) on the Dejpeg task by using different training datasets.

TrainingSet	Classic5[14]			
	10	20	30	40
BSDS400+WED	30.27	32.25	33.69	34.52
HQ-50K	30.34	32.44	33.72	34.56

Table 7. Results comparison on the deraining task by using different training datasets.

Method	TrainingSet	Rain100L[52]		Rain100H[52]	
		PSNR	SSIM	PSNR	SSIM
Restormer[56]	Rain13K	38.99	0.9780	31.46	0.9040
SwinIR[31]	Rain13K	35.97	0.9640	29.80	0.8827
SwinIR[31]	HQ-50K	41.86	0.9894	32.52	0.9257

the weighted summation of different experts:

$$y = \sum_i^n w(x)_i E_i(x), \quad (1)$$

where $w(x) \in \mathbb{R}^n$ is the weight of different experts for the input x . In this paper, we design two types of MoE layers, named as H-MoE and S-MoE, as illustrated in Figure 5 (b) and (c). The key difference between the two is in their routing strategy. For H-MoE (Hard-MoE), $w(x)$ is represented as a one-hot vector. This means that the input feature x is only visible to the corresponding task-specific expert. In contrast, for S-MoE (Soft-MoE), $w(x)$ is obtained through a gating network:

$$w(x) = \mathcal{Z}_k(\text{softmax}(\mathbf{W}_g \otimes x_i)), \quad (2)$$

where $\mathbf{W}_g \in \mathbb{R}^{n \times C}$ is a trainable parameter, \otimes is the matrix multiplication, $\mathcal{Z}_k(\cdot)$ is the function that sets all values to zeros except the top- k largest values.

4.2. Mixture of Expert Block

Equipped with the H-MoE and S-MoE layers described above, we design two types of MoE blocks accordingly. As

Table 8. Multi-task results using a unified model trained on both our HQ-50K and the combination of existing restoration datasets from all the tasks involved. The best results are in bold.

Training Set	Method	SR (PSNR-Y)			DeRain (PSNR-Y)	Denoise (PSNR)			Dejpeg (PSNR)			
		Manga109			Rain100L	CBSD68			Classic5			
		x2	x3	x4	-	15	25	50	40	30	20	10
Combination	AirNet[27]	36.98	25.02	23.24	31.20	33.50	30.67	26.35	33.73	32.88	31.58	29.25
	SwinIR[31]	36.72	31.52	25.78	36.28	33.82	31.19	27.89	33.77	32.91	30.75	29.39
	DAMoE	37.95	32.93	25.89	38.04	34.12	31.47	28.22	34.00	33.16	31.87	29.67
HQ-50K	AirNet[27]	37.13	25.11	23.37	35.31	33.63	30.78	26.53	33.86	33.01	31.75	29.54
	SwinIR [31]	37.56	32.48	25.87	38.08	34.05	31.38	28.09	33.94	33.10	31.83	29.61
	DAMoE	38.51	33.40	26.12	40.22	34.18	31.52	28.28	34.15	33.31	32.03	29.80

shown in Figure 6 (a) and (b), we replace the FFN layer in the original transformer block with these two types of MoE layers. In the *H-MoE block*, the number of experts is the same as the number of tasks, with each expert responsible for one task. Different tasks have no mutual influence within the H-MoE layer. Note that we share the same expert for different degradation levels of one task. In the *S-MoE block*, the number of experts in the S-MoE layer is a hyperparameter and does not need to be the same as the number of tasks. The S-MoE block learns how to use different combinations of experts for different tasks and degradation levels. DAMoE can use one type of MoE block or a combination of both by alternating between the H-MoE and S-MoE blocks. A detailed performance analysis will be provided in the ablation analysis section.

5. Experiments

Experiment Setup. We conduct experiments on four representative image restoration tasks including SR, deraining, dejpeg and denoising. We train the models on both our HQ-50K and existing restoration datasets, and compare the performance. As the baseline, for SR, we use the DF2K dataset, which is a combination of DIV2K [2] and Flickr2K [32]). For deraining, we use the Rain13K dataset, which is a combination of Rain14000 [23], Rain1800 [53], Rain800 [60], and Rain12 [30]. For denoising and dejpeg, we use the combination of BSD400 [4] and WED [35] as the training set.

To create training image pairs, we follow the standard setting[27, 31, 56] and consider different degradations as follows: 1) For SR, bicubic is used to obtain downsampled image; 2) For denoising, we add white Gaussian noise with $\sigma = \{15, 25, 50\}$ to the color images; 3) For dejpeg, we compress images with JPEG quality $q = \{10, 20, 30, 40\}$; 4) For deraining, we use the synthetic rain method [52] to create the corresponding raining image.

5.1. Evaluation on Single Task

We first show the quantitative results of our proposed HQ-50K on each single image restoration task. Here we uniformly use SwinIR [31] as the training framework. Ta-

Table 9. Ablating the four aspects in dataset requirements on $\times 2$ SR task. The ablated aspect in each row is marked with blue color.

Res.	H-freq	Bpp	Div.	Manga109[17]	
				PSNR	SSIM
279,948	0.0183	12.34	1.143	37.88	0.9758
2,519,300	0.0011	12.86	1.143	35.51	0.9663
2,519,300	0.0134	1.88	1.143	34.10	0.9521
2,513,121	0.0189	12.92	1.001	39.17	0.9780
2,519,300	0.0185	12.92	1.143	39.54	0.9791

ble 3 shows the performance comparison on the SR task, as we can see, significant performance gain can be obtained on both the Set14 and Manga109 dataset by using our HQ-50K. In Table 4, We further present the detailed performance analysis on our proposed fine-grained evaluation benchmark to evaluate the performance on different semantic categories. Due to the limited number of artificial images in DF2K compared to our HQ-50K dataset, which has a more balanced semantic coverage, the model trained on HQ-50K performs significantly better on artificial images. This highlights the importance of semantic coverage and balance when training a generalizable SR model.

For the denoising, dejpeg and deraining tasks, the corresponding results are presented in Table 5, Table 6 and Table 7 respectively. It can be seen that, our proposed HQ-50K can also achieve consistently better results than the existing restoration datasets or their combination. Especially on the deraining task, the model trained on our HQ-50K outperforms the baseline by a large margin on Rain100L benchmark (i.e., more than 5 dB).

5.2. Evaluation on Multiple Tasks

In addition to the single task evaluation, we further provide the multi-task evaluation results with existing unified restoration models. Here we choose AirNet [27] and SwinIR [31] as the baselines. In detail, though AirNet [27] gave the results of processing different unknown degradation with one unified model, it has not covered the experiments on SR and dejpeg tasks. And SwinIR [31] only provided results of the single task setting to handle a specified task and degradation level. Therefore, we run their officially released code to report the results by following

Table 10. Ablation Study for the effect of different MoE Structure on All-in-One Training.

	H-MoE	S-MoE	Params(M)	FLOPs(G)	SR $\times 2$		Derain		Denoise 15	Dejpeg 40
					Manga109 [17] PSNR	SSIM	Rain100L [52] PSNR	SSIM	CBSD68 [36] PSNR	Classic5 [14] PSNR
SwinIR	-	-	11.49	83.49	37.56	0.9748	38.08	0.9798	34.05	33.94
	✓	-	25.55	83.49	37.72	0.9754	38.12	0.9801	34.08	33.95
	-	✓	139.05	99.98	37.90	0.9760	38.30	0.9809	34.11	34.03
	✓	✓	82.30	91.74	38.51	0.9772	40.22	0.9861	34.18	34.15

Table 11. The impact of multi-task training on a single model. Multi-task means inputs are in different tasks, while multi-level means inputs with different degradation levels.

DAMoE	Multi-task	Multi-level	SR $\times 2$		DeRain	Denoise $\sigma = 15$	Dejpeg $q = 40$
			Manga109 [17] PSNR/SSIM	SSIM	Rain100L [52] PSNR/SSIM	CBSD68 [36] PSNR	Classic5 [14] PSNR
-	-	-	40.05/0.9894		41.86/0.9894	34.38	34.56
-	-	✓	37.91/0.9769		-	34.17	34.08
-	✓	✓	37.56/0.9748		38.08/0.9798	34.05	33.94
✓	✓	✓	38.51/0.9772		40.22/0.9860	34.18	34.15

the default settings. We train these baseline models and our DAMoE model on both our HQ-50K and the combination of existing restoration datasets from all the tasks involved. The detailed results are shown in Table 8. Comparing the results between using our HQ-50K and the combination of existing datasets, we can observe consistent performance improvement on all different tasks, demonstrating the value of our dataset for training a unified restoration model. On the other hand, when using the same training dataset, our proposed unified model DAMoE also outperforms existing state-of-the-art unified restoration model AirNet [27]. This shows that integrating the MoE idea for unifying different restoration tasks is a very promising direction and worthy of further investigation.

5.3. Ablation Analysis

Ablation of data requirements. In Section 3, we have already provided the detailed analysis of existing datasets from the proposed five aspects. In this section, we further provide the ablation results on our HQ-50K. Since the performance trend for different data scales is already given in Figure 2, we only provide the ablation results on other four aspects in Table 9. Considering the training resource, here we only use a subset of 800 images from HQ-50K for each ablation setting. From the ablation results, we can see that all the four aspects are very important for our HQ-50K and without considering any of each aspect will result in significant performance drop on the SR task.

MoE block design. As previously described, we have developed two types of MoE blocks. Table 10 presents an analysis of the performance of different MoE block options. Specifically, we used SwinIR as the baseline and tested three configurations: 1) SwinIR with only H-MoE block; 2) SwinIR with only S-MoE block, where the expert number of S-MoE layer is set to 16; 3) SwinIR with

both S-MoE and H-MoE blocks arranged alternately. We observe that both H-MoE and S-MoE significantly enhance performance when compared to the baseline. For H-MoE, the FLOPs remain constant, but the number of parameters increases. For S-MoE, both the number of parameters and FLOPs greatly increase. When H-MoE and S-MoE are alternated, the performance further improves while achieving a better balance between H-MoE and S-MoE in terms of parameter number and FLOPs. Therefore, we default to using this alternated design.

Single to multiple tasks. In this experiment, we want to study the performance influence of the multi-task and multi-level support in the unified model. In Table 11, we use the SwinIR trained on each specific task and degradation level as the baseline. It shows that, despite the flexibility, using one unified model to support multiple restoration tasks and multiple degradation levels will both result in the performance drop for each specific evaluation setting. By integrating the MoE mechanism that uses different experts to decouple different tasks, our proposed DAMoE can greatly improve the performance.

6. Conclusions and Limitations

In this paper, we present HQ-50K, a large-scale, high-quality dataset that is suitable for various image restoration tasks. This effort is crucial in advancing image restoration tasks to a larger scale and unlocking the full potential of restoration models. While the number of images in HQ-50K is larger than most existing low-level datasets, it is still several orders of magnitude smaller than datasets designed for other understanding tasks, such as Laion-5B [41] for multimodal pretraining. In the near future, we plan to further expand the dataset to an even larger scale. Based on HQ-50K, we also propose a unified restoration model DAMoE, which incorporates the mix of expert idea to han-

dle different restoration tasks simultaneously. Our extensive experimental results demonstrate the value of our proposed dataset and unified model.

References

- [1] Abdelrahman Abdelhamed, Stephen Lin, and Michael S Brown. A high-quality denoising dataset for smartphone cameras. In *Proceedings of the IEEE Conference on Computer Vision and Pattern Recognition*, pages 1692–1700, 2018. 2
- [2] E. Agustsson and R. Timofte. Ntire 2017 challenge on single image super-resolution: Dataset and study. In *2017 IEEE Conference on Computer Vision and Pattern Recognition Workshops (CVPRW)*, 2017. 1, 2, 3, 5, 7, 12
- [3] Saeed Anwar and Nick Barnes. Real image denoising with feature attention. In *Proceedings of the IEEE/CVF international conference on computer vision*, pages 3155–3164, 2019. 2
- [4] Siavash Arjomand Bigdeli, Matthias Zwicker, Paolo Favaro, and Meiguang Jin. Deep mean-shift priors for image restoration. *Advances in Neural Information Processing Systems*, 30, 2017. 1, 2, 5, 7
- [5] Dongdong Chen, Qingnan Fan, Jing Liao, Angelica Aviles-Rivero, Lu Yuan, Nenghai Yu, and Gang Hua. Controllable image processing via adaptive filterbank pyramid. *IEEE Transactions on Image Processing*, 29:8043–8054, 2020. 2, 3
- [6] Dongdong Chen, Mingming He, Qingnan Fan, Jing Liao, Liheng Zhang, Dongdong Hou, Lu Yuan, and Gang Hua. Gated context aggregation network for image dehazing and deraining. In *2019 IEEE winter conference on applications of computer vision (WACV)*, pages 1375–1383. IEEE, 2019. 2, 3
- [7] Hanting Chen, Yunhe Wang, Tianyu Guo, Chang Xu, Yiping Deng, Zhenhua Liu, Siwei Ma, Chunjing Xu, Chao Xu, and Wen Gao. Pre-trained image processing transformer. In *Proceedings of the IEEE/CVF Conference on Computer Vision and Pattern Recognition*, pages 12299–12310, 2021. 2, 3
- [8] Liangyu Chen, Xiaojie Chu, Xiangyu Zhang, and Jian Sun. Simple baselines for image restoration. *arXiv preprint arXiv:2204.04676*, 2022. 3
- [9] Liangyu Chen, Xin Lu, Jie Zhang, Xiaojie Chu, and Chengpeng Chen. Hinet: Half instance normalization network for image restoration. In *Proceedings of the IEEE/CVF Conference on Computer Vision and Pattern Recognition*, pages 182–192, 2021. 3
- [10] Wei-Ting Chen, Zhi-Kai Huang, Cheng-Che Tsai, Hao-Hsiang Yang, Jian-Jiun Ding, and Sy-Yen Kuo. Learning multiple adverse weather removal via two-stage knowledge learning and multi-contrastive regularization: Toward a unified model. In *Proceedings of the IEEE/CVF Conference on Computer Vision and Pattern Recognition*, pages 17653–17662, 2022. 3
- [11] Tao Dai, Jianrui Cai, Yongbing Zhang, Shu-Tao Xia, and Lei Zhang. Second-order attention network for single image super-resolution. In *Proceedings of the IEEE/CVF conference on computer vision and pattern recognition*, pages 11065–11074, 2019. 2
- [12] Chao Dong, Chen Change Loy, Kaiming He, and Xiaoou Tang. Image super-resolution using deep convolutional networks. *IEEE transactions on pattern analysis and machine intelligence*, 38(2):295–307, 2015. 2
- [13] William Fedus, Barret Zoph, and Noam Shazeer. Switch transformers: Scaling to trillion parameter models with simple and efficient sparsity, 2021. 3, 6
- [14] Alessandro Foi, Vladimir Katkovnik, and Karen Egiazarian. Pointwise shape-adaptive dct for high-quality denoising and deblocking of grayscale and color images. *IEEE transactions on image processing*, 16(5):1395–1411, 2007. 6, 8, 15
- [15] Rich Franzen. Kodak lossless true color image suite. *source: http://r0k.us/graphics/kodak*, 4(2), 1999. 6
- [16] Xueyang Fu, Jiabin Huang, Xinghao Ding, Yinghao Liao, and John Paisley. Clearing the skies: A deep network architecture for single-image rain removal. *IEEE Transactions on Image Processing*, 26(6):2944–2956, 2017. 3
- [17] Azuma Fujimoto, Toru Ogawa, Kazuyoshi Yamamoto, Yusuke Matsui, Toshihiko Yamasaki, and Kiyoharu Aizawa. Manga109 dataset and creation of metadata. In *Proceedings of the 1st international workshop on comics analysis, processing and understanding*, pages 1–5, 2016. 3, 7, 8, 16
- [18] Xiaowei Hu, Chi-Wing Fu, Lei Zhu, and Pheng-Ann Heng. Depth-attentional features for single-image rain removal. In *Proceedings of the IEEE/CVF Conference on Computer Vision and Pattern Recognition*, pages 8022–8031, 2019. 3
- [19] Jia-Bin Huang, Abhishek Singh, and Narendra Ahuja. Single image super-resolution from transformed self-exemplars. In *Proceedings of the IEEE conference on computer vision and pattern recognition*, pages 5197–5206, 2015. 4
- [20] Robert A Jacobs, Michael I Jordan, Steven J Nowlan, and Geoffrey E Hinton. Adaptive mixtures of local experts. *Neural computation*, 3(1):79–87, 1991. 6
- [21] D. Jia, D. Wei, R. Socher, L. J. Li, L. Kai, and F. F. Li. Imagenet: A large-scale hierarchical image database. pages 248–255, 2009. 1, 2, 3, 5, 14
- [22] Kui Jiang, Zhongyuan Wang, Peng Yi, Chen Chen, Baojin Huang, Yimin Luo, Jiayi Ma, and Junjun Jiang. Multi-scale progressive fusion network for single image deraining. In *Proceedings of the IEEE/CVF conference on computer vision and pattern recognition*, pages 8346–8355, 2020. 2
- [23] Tai-Xiang Jiang, Ting-Zhu Huang, Xi-Le Zhao, Liang-Jian Deng, and Yao Wang. A novel tensor-based video rain streaks removal approach via utilizing discriminatively intrinsic priors. In *Proceedings of the IEEE conference on computer vision and pattern recognition*, pages 4057–4066, 2017. 2, 7
- [24] Jiwon Kim, Jung Kwon Lee, and Kyoung Mu Lee. Accurate image super-resolution using very deep convolutional networks. In *Proceedings of the IEEE conference on computer vision and pattern recognition*, pages 1646–1654, 2016. 2
- [25] Wei-Sheng Lai, Jia-Bin Huang, Narendra Ahuja, and Ming-Hsuan Yang. Deep laplacian pyramid networks for fast and accurate super-resolution. In *Proceedings of the IEEE conference on computer vision and pattern recognition*, pages 624–632, 2017. 2
- [26] Dmitry Lepikhin, HyoukJoong Lee, Yuanzhong Xu, Dehao Chen, Orhan Firat, Yanping Huang, Maxim Krikun, Noam

- Shazeer, and Zhifeng Chen. Gshard: Scaling giant models with conditional computation and automatic sharding. *arXiv preprint arXiv:2006.16668*, 2020. 3
- [27] Boyun Li, Xiao Liu, Peng Hu, Zhongqin Wu, Jiancheng Lv, and Xi Peng. All-in-one image restoration for unknown corruption. In *Proceedings of the IEEE/CVF Conference on Computer Vision and Pattern Recognition*, pages 17452–17462, 2022. 3, 7, 8
- [28] Ke Li, Bahetiyaer Bare, and Bo Yan. An efficient deep convolutional neural networks model for compressed image deblocking. In *2017 IEEE International Conference on Multimedia and Expo (ICME)*, pages 1320–1325. IEEE, 2017. 2
- [29] Wenbo Li, Xin Lu, Jiangbo Lu, Xiangyu Zhang, and Jiaya Jia. On efficient transformer and image pre-training for low-level vision. *arXiv preprint arXiv:2112.10175*, 2021. 2, 3
- [30] Yu Li, Robby T Tan, Xiaojie Guo, Jiangbo Lu, and Michael S Brown. Rain streak removal using layer priors. In *Proceedings of the IEEE conference on computer vision and pattern recognition*, pages 2736–2744, 2016. 7
- [31] Jingyun Liang, Jiezhong Cao, Guolei Sun, Kai Zhang, Luc Van Gool, and Radu Timofte. Swinir: Image restoration using swin transformer. In *Proceedings of the IEEE/CVF International Conference on Computer Vision*, pages 1833–1844, 2021. 3, 6, 7, 12
- [32] B. Lim, S. Son, H. Kim, S. Nah, and K. M. Lee. Enhanced deep residual networks for single image super-resolution. *IEEE*, 2017. 1, 2, 5, 7
- [33] Tsung-Yi Lin, Michael Maire, Serge Belongie, James Hays, Pietro Perona, Deva Ramanan, Piotr Dollár, and C Lawrence Zitnick. Microsoft coco: Common objects in context. In *Computer Vision—ECCV 2014: 13th European Conference, Zurich, Switzerland, September 6–12, 2014, Proceedings, Part V 13*, pages 740–755. Springer, 2014. 1
- [34] Ze Liu, Yutong Lin, Yue Cao, Han Hu, Yixuan Wei, Zheng Zhang, Stephen Lin, and Baining Guo. Swin transformer: Hierarchical vision transformer using shifted windows. In *Proceedings of the IEEE/CVF International Conference on Computer Vision*, pages 10012–10022, 2021. 6
- [35] Kede Ma, Zhengfang Duanmu, Qingbo Wu, Zhou Wang, Hongwei Yong, Hongliang Li, and Lei Zhang. Waterloo exploration database: New challenges for image quality assessment models. *IEEE Transactions on Image Processing*, 26(2):1004–1016, 2016. 1, 2, 5, 7
- [36] David Martin, Charless Fowlkes, Doron Tal, and Jitendra Malik. A database of human segmented natural images and its application to evaluating segmentation algorithms and measuring ecological statistics. In *Proceedings Eighth IEEE International Conference on Computer Vision. ICCV 2001*, volume 2, pages 416–423. IEEE, 2001. 6, 8, 15, 16
- [37] Ben Niu, Weilei Wen, Wenqi Ren, Xiangde Zhang, Lianping Yang, Shuzhen Wang, Kaihao Zhang, Xiaochun Cao, and Haifeng Shen. Single image super-resolution via a holistic attention network. In *European conference on computer vision*, pages 191–207. Springer, 2020. 2
- [38] Alec Radford, Jong Wook Kim, Chris Hallacy, Aditya Ramesh, Gabriel Goh, Sandhini Agarwal, Girish Sastry, Amanda Askell, Pamela Mishkin, Jack Clark, et al. Learning transferable visual models from natural language supervision. In *International conference on machine learning*, pages 8748–8763. PMLR, 2021. 4
- [39] Dongwei Ren, Wangmeng Zuo, Qinghua Hu, Pengfei Zhu, and Deyu Meng. Progressive image deraining networks: A better and simpler baseline. In *Proceedings of the IEEE/CVF Conference on Computer Vision and Pattern Recognition*, pages 3937–3946, 2019. 2
- [40] Carlos Riquelme, Joan Puigcerver, Basil Mustafa, Maxim Neumann, Rodolphe Jenatton, André Susano Pinto, Daniel Keysers, and Neil Houlsby. Scaling vision with sparse mixture of experts. *Advances in Neural Information Processing Systems*, 34:8583–8595, 2021. 3
- [41] Christoph Schuhmann. Laion-400-million open dataset, 2021. 2, 3, 4, 8, 14
- [42] Noam Shazeer, Azalia Mirhoseini, Krzysztof Maziarz, Andy Davis, Quoc Le, Geoffrey Hinton, and Jeff Dean. Outrageously large neural networks: The sparsely-gated mixture-of-experts layer. *arXiv preprint arXiv:1701.06538*, 2017. 3, 6
- [43] HR Sheikh. Live image quality assessment database release 2. <http://live.ece.utexas.edu/research/quality>, 2005. 16
- [44] Wenzhe Shi, Jose Caballero, Ferenc Huszár, Johannes Totz, Andrew P Aitken, Rob Bishop, Daniel Rueckert, and Zehan Wang. Real-time single image and video super-resolution using an efficient sub-pixel convolutional neural network. In *Proceedings of the IEEE conference on computer vision and pattern recognition*, pages 1874–1883, 2016. 2
- [45] Pranjay Shyam, Kyung-Soo Kim, and Kuk-Jin Yoon. Giqe: Generic image quality enhancement via nth order iterative degradation. In *Proceedings of the IEEE/CVF Conference on Computer Vision and Pattern Recognition*, pages 2077–2087, 2022. 3
- [46] Zhengzhong Tu, Hossein Talebi, Han Zhang, Feng Yang, Peyman Milanfar, Alan Bovik, and Yinxiao Li. Maxim: Multi-axis mlp for image processing. In *Proceedings of the IEEE/CVF Conference on Computer Vision and Pattern Recognition*, pages 5769–5780, 2022. 3
- [47] Jeya Maria Jose Valanarasu, Rajeev Yasarla, and Vishal M Patel. Transweather: Transformer-based restoration of images degraded by adverse weather conditions. In *Proceedings of the IEEE/CVF Conference on Computer Vision and Pattern Recognition*, pages 2353–2363, 2022. 3
- [48] Zhendong Wang, Xiaodong Cun, Jianmin Bao, and Jianzhuang Liu. Uformer: A general u-shaped transformer for image restoration. *arXiv preprint arXiv:2106.03106*, 2021. 3
- [49] Wei Wei, Deyu Meng, Qian Zhao, Zongben Xu, and Ying Wu. Semi-supervised transfer learning for image rain removal. In *Proceedings of the IEEE/CVF conference on computer vision and pattern recognition*, pages 3877–3886, 2019. 3
- [50] Lemeng Wu, Mengchen Liu, Yinpeng Chen, Dongdong Chen, Xiyang Dai, and Lu Yuan. Residual mixture of experts. *arXiv preprint arXiv:2204.09636*, 2022. 3

- [51] Jun Xu, Hui Li, Zhetong Liang, David Zhang, and Lei Zhang. Real-world noisy image denoising: A new benchmark. *arXiv preprint arXiv:1804.02603*, 2018. [2](#)
- [52] Wenhan Yang, Robby T Tan, Jiashi Feng, Jiaying Liu, Zongming Guo, and Shuicheng Yan. Deep joint rain detection and removal from a single image. In *Proceedings of the IEEE conference on computer vision and pattern recognition*, pages 1357–1366, 2017. [1](#), [2](#), [6](#), [7](#), [8](#), [16](#)
- [53] Wenhan Yang, Robby T Tan, Jiashi Feng, Jiaying Liu, Zongming Guo, and Shuicheng Yan. Deep joint rain detection and removal from a single image. In *Proceedings of the IEEE conference on computer vision and pattern recognition*, pages 1357–1366, 2017. [7](#)
- [54] Chia-Hung Yeh, Chu-Han Lin, Min-Hui Lin, Li-Wei Kang, Chih-Hsiang Huang, and Mei-Juan Chen. Deep learning-based compressed image artifacts reduction based on multi-scale image fusion. *Information Fusion*, 67:195–207, 2021. [2](#)
- [55] Zongsheng Yue, Hongwei Yong, Qian Zhao, Deyu Meng, and Lei Zhang. Variational denoising network: Toward blind noise modeling and removal. *Advances in neural information processing systems*, 32, 2019. [2](#)
- [56] Syed Waqas Zamir, Aditya Arora, Salman Khan, Munawar Hayat, Fahad Shahbaz Khan, and Ming-Hsuan Yang. Restormer: Efficient transformer for high-resolution image restoration. In *Proceedings of the IEEE/CVF Conference on Computer Vision and Pattern Recognition*, pages 5728–5739, 2022. [3](#), [6](#), [7](#)
- [57] Syed Waqas Zamir, Aditya Arora, Salman Khan, Munawar Hayat, Fahad Shahbaz Khan, Ming-Hsuan Yang, and Ling Shao. Learning enriched features for real image restoration and enhancement. In *Computer Vision—ECCV 2020: 16th European Conference, Glasgow, UK, August 23–28, 2020, Proceedings, Part XXV 16*, pages 492–511. Springer, 2020. [3](#)
- [58] Syed Waqas Zamir, Aditya Arora, Salman Khan, Munawar Hayat, Fahad Shahbaz Khan, Ming-Hsuan Yang, and Ling Shao. Multi-stage progressive image restoration. In *Proceedings of the IEEE/CVF conference on computer vision and pattern recognition*, pages 14821–14831, 2021. [1](#), [2](#), [5](#)
- [59] He Zhang and Vishal M Patel. Density-aware single image de-raining using a multi-stream dense network. In *Proceedings of the IEEE conference on computer vision and pattern recognition*, pages 695–704, 2018. [2](#)
- [60] He Zhang, Vishwanath Sindagi, and Vishal M Patel. Image de-raining using a conditional generative adversarial network. *IEEE transactions on circuits and systems for video technology*, 30(11):3943–3956, 2019. [1](#), [2](#), [7](#)
- [61] Kai Zhang, Wangmeng Zuo, Yunjin Chen, Deyu Meng, and Lei Zhang. Beyond a gaussian denoiser: Residual learning of deep cnn for image denoising. *IEEE transactions on image processing*, 26(7):3142–3155, 2017. [1](#), [3](#)
- [62] Kai Zhang, Wangmeng Zuo, and Lei Zhang. Ffdnet: Toward a fast and flexible solution for cnn-based image denoising. *IEEE Transactions on Image Processing*, 27(9):4608–4622, 2018. [3](#)
- [63] Yulun Zhang, Kunpeng Li, Kai Li, Lichen Wang, Bineng Zhong, and Yun Fu. Image super-resolution using very deep residual channel attention networks. In *Proceedings of the European conference on computer vision (ECCV)*, pages 286–301, 2018. [2](#)

A. DataSet

A.1. Rich Texture Details

As emphasized in our main text, the level of detail in the image’s texture plays a crucial role in determining the quality of a dataset. To accurately measure this, we employ a quantitative method by calculating the high-frequency ratio of each image. This ratio indicates the proportion of high-frequency components in the image, which directly correlates with the richness of texture details. To calculate the high-frequency ratio, we begin by mapping the image to the frequency domain using Discrete Fourier Transform (DFT), as shown in Equation (3). Next, we apply the Ideal High-pass Filter (IHPF), represented by Equation (5), to extract the high-frequency components of the image. Finally, we compute the ratio of the power spectrum of the high-frequency components, as given by Equation (6).

$$F(u, v) = \frac{1}{HW} \sum_{x=0}^{H-1} \sum_{y=0}^{W-1} f(x, y) e^{-2j\pi(ux/H+vy/W)} \quad (3)$$

where H, W is the height and width of the image, $f(x, y)$ is the gray value corresponding to the pixel with coordinates (x, y) .

$$D(u, v) = [(u - \frac{H}{2})^2 + (v - \frac{W}{2})^2]^{\frac{1}{2}} \quad (4)$$

$$H(u, v) = \begin{cases} 0, & D(u, v) \leq D_0 \\ 1, & D(u, v) > D_0 \end{cases} \quad (5)$$

$$ratio = \frac{\sum_{(u,v)} |H(u, v) \cdot F(u, v)|^2}{\sum_{(u,v)} |F(u, v)|^2} \quad (6)$$

where $D(u, v)$ is the distance between the frequency point (u, v) and the center of the frequency domain $(\frac{H}{2}, \frac{W}{2})$, D_0 is the cutoff frequency of the ideal high-pass filter, in this paper, we set $D_0 = \frac{1}{2} \sqrt{(\frac{H}{2})^2 + (\frac{W}{2})^2}$

A.2. Semantic Coverage

In our main text, we discussed how the existing restoration datasets have inferior semantic coverage compared to our dataset, especially for the artificial images. In Figure 7, we present a detailed distribution of the image numbers across different semantic sub-categories for both our dataset and the existing ones. It can be seen that there is few or no images for the subclass of map, comic or posters in existing restoration datasets. Besides, we also maintain a better balance of different sub-categories in our HQ-50K to avoid the performance bias. In Table 12, we show the detailed performance of SwinIR trained on DIV2K and our HQ-50K for each sub-category (The summarized average

performance is reported in Table 4 in our main text). It can be observed that the performance gap of the model trained on our HQ-50K and DIV2K [2] is significantly larger on the artificial subclass due to the limited artificial image coverage of DIV2K [2].

Note that due to the diverse semantic categories, it is challenging to categorize each image into a well-defined category set. For images that do not belong to these sub-categories, we classify them into “others” For instance, for Outdoor, “others” include traffic lights, road sign devices, carry-on items, *etc.*; for Indoor, “others” includes knitting textures, electronic devices *etc.*; for Artificial, “others” include game interfaces, handwriting, screen shots *etc.*

For the fine-grained test benchmark we proposed, we give some visualization examples in Figure 8. Except for the text scene, which contains 50 test images, all other 12 sub-categories have 100 test images.

B. Network Structure

B.1. Detailed Network Architectures

In this section, we will provide a detailed explanation of our DAMoE network framework for unified restoration. A total of 11 degradations are involved in our unified training, including SR for $\times 2, \times 3, \times 4$, deraining, denoising for $\sigma = \{15, 25, 50\}$, dejpeg for $q = \{10, 20, 30, 40\}$. The overall structure is shown in Figure 9, where the number of MoE-conv Blocks L , the number of MoE blocks D , the input size, window size, channel number C and attention head number are set to 6, 6, 84×84 , 7, 180 and 6 respectively. In H-MoE (Hard-MoE), the number of experts is the same as the number of tasks, which is 4 in our experiment, while the number of SMoE (Soft-MoE) is set to 16 to achieve a trade-off of performance and computing cost.

B.2. Detailed Design of HMoE and SMoE

During our early attempts, we found that a simple combination of Transformer and MoE layers did not perform well in low-level tasks. The possible reason is that, in the backbone SwinIR [31] that we select as a baseline, each token corresponds to a pixel rather than a patch, when it comes to the gating network of MoE, the input token corresponding to a single pixel is too small to be conducive to the selection of the gating. Without gating constraints, it was more challenging for the model to converge compared to the typical patch-wise tokens. To address this issue, we first simplified the MoE design to HMoE. In H-MoE, the input feature x is visible only to the corresponding task-specific expert, avoiding the problem of limited receptive field of the gating network.

To take advantage of gating strategy and solve the problem, we further propose patch-level tokens in SMoE. In detail, as Figure 9 (b) shows, given the 2D feature maps

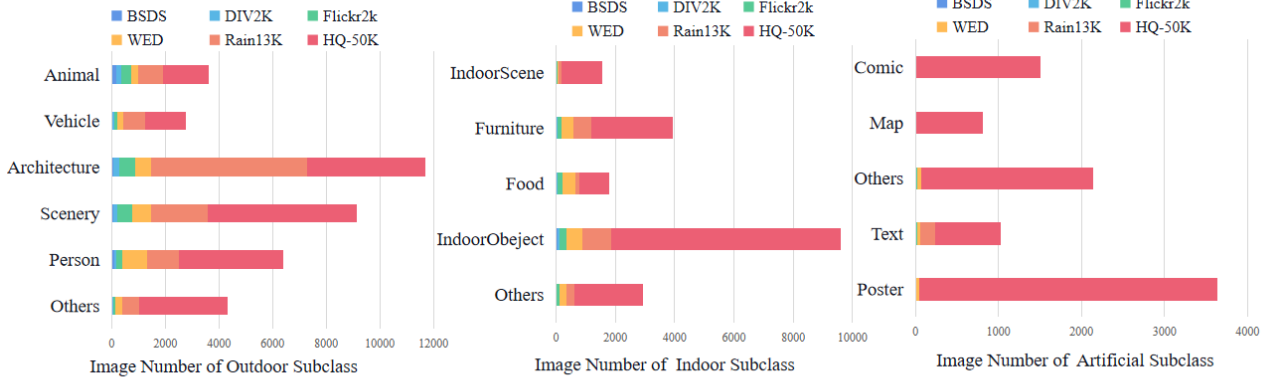


Figure 7. Semantic distribution of datasets. (a), (b), (c) show the image number of each subclass in Outdoor, Indoor, Artificial class respectively.

Table 12. Comparison of the SR results trained on DIV2K and our HQ-50K on our fine-grained evaluation benchmark: Outdoor(top), Indoor(middle), Artificial(bottom).

Scale	TrainingSet	Animals		People		Nature		Transportation		Architecture		Outdoor	
		PSNR	SSIM	PSNR	SSIM	PSNR	SSIM	PSNR	SSIM	PSNR	SSIM	PSNR	SSIM
x2	DIV2K	35.30	0.9169	30.19	0.8907	28.07	0.8770	31.47	0.9206	28.84	0.8988	30.78	0.9008
	HQ-50K	35.40	0.9194	30.50	0.8979	28.20	0.8827	31.67	0.9256	29.23	0.9078	31.00	0.9067
x3	DIV2K	31.68	0.8337	27.22	0.7995	25.05	0.7540	28.14	0.8413	25.63	0.7939	27.54	0.8045
	HQ-50K	31.84	0.8352	27.34	0.8032	25.10	0.7569	28.31	0.8447	25.88	0.8029	27.69	0.8086
x4	DIV2K	29.81	0.7724	25.80	0.7368	23.67	0.6642	26.50	0.7809	24.08	0.7126	25.97	0.7334
	HQ-50K	29.99	0.7775	25.98	0.7413	23.78	0.6680	26.74	0.7862	24.39	0.7214	26.18	0.7389

Scale	TrainingSet	Indoor Scenes		Furniture		Food		Indoor Object		Indoor	
		PSNR	SSIM	PSNR	SSIM	PSNR	SSIM	PSNR	SSIM	PSNR	SSIM
x2	DIV2K	31.56	0.9079	30.63	0.9091	33.73	0.9207	28.93	0.8835	31.21	0.9053
	HQ-50K	31.90	0.9129	31.12	0.9176	33.91	0.9272	29.15	0.8961	31.52	0.9134
x3	DIV2K	28.43	0.8316	27.51	0.8289	30.37	0.8476	25.68	0.7721	28.00	0.8201
	HQ-50K	28.63	0.8321	27.80	0.8311	30.51	0.8501	25.90	0.7765	28.21	0.8224
x4	DIV2K	26.84	0.7757	25.96	0.7686	28.68	0.7925	24.12	0.6862	26.40	0.7558
	HQ-50K	27.01	0.7811	26.24	0.7762	28.82	0.7951	24.36	0.6934	26.60	0.7614
Scale	TrainingSet	Comic		Poster		Map		Text Scene		Artificial	
		PSNR	SSIM	PSNR	SSIM	PSNR	SSIM	PSNR	SSIM	PSNR	SSIM
x2	DIV2K	31.10	0.9418	32.22	0.8977	27.77	0.9053	29.96	0.8941	30.31	0.9120
	HQ-50K	31.35	0.9600	32.46	0.9178	28.06	0.9172	30.01	0.9072	30.47	0.9256
x3	DIV2K	26.72	0.8864	28.96	0.8302	24.17	0.8163	26.82	0.8029	26.65	0.8384
	HQ-50K	27.86	0.8997	29.45	0.8355	25.26	0.8356	27.18	0.8114	27.47	0.8504
x4	DIV2K	24.23	0.8314	27.25	0.7841	22.58	0.7439	25.44	0.7406	24.79	0.7799
	HQ-50K	25.38	0.8520	27.79	0.7915	23.41	0.7697	25.72	0.7499	25.55	0.7966

$X \in \mathbb{R}^{C \times H \times W}$, where H and W are the height and width of the feature, we first split X into no-overlapping patches with the patch size of $P \times P$, and then obtain the i th flatten embedding $x_i \in \mathbb{R}^{P^2 \times C}$ from each patch i :

$$X = \{x_1, x_2, \dots, x_N\}, N = HW/P^2 \quad (7)$$

(8)

Then for each x_i , we feed it into SMOE:

$$w_i = \mathcal{Z}_k(\text{softmax}(\mathbf{W}_g \otimes x_i)), \quad (9)$$

$$y_i = \sum_j^n w(x_i)_j E_j(x_i), \quad (10)$$

$$Y = \{y_1, y_2, \dots, y_N\}, N = HW/P^2 \quad (11)$$

where n is the number of expert, $w_i \in \mathbb{R}^n$ is the weight

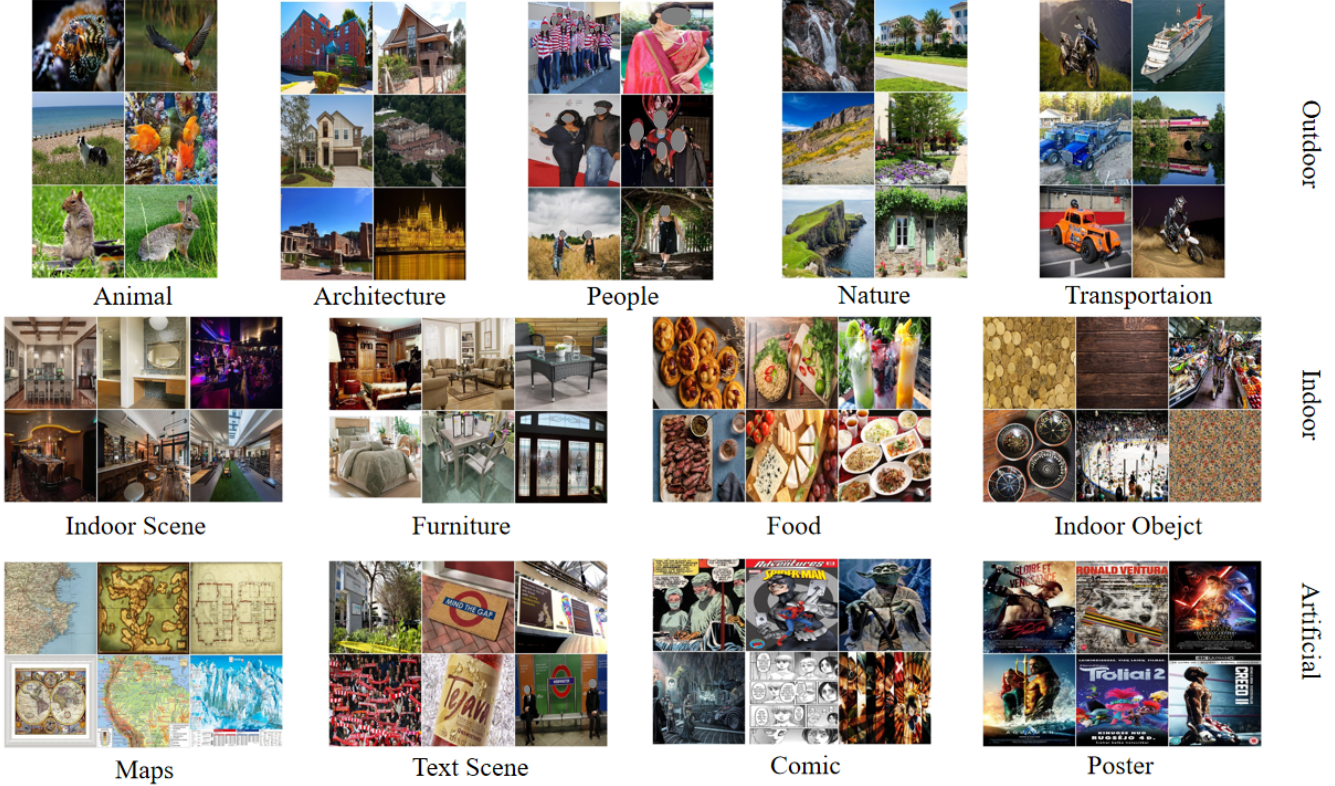


Figure 8. Example images in our fine-grained benchmark dataset. From top to down are the images of Outdoor, Indoor, and Artificial respectively.

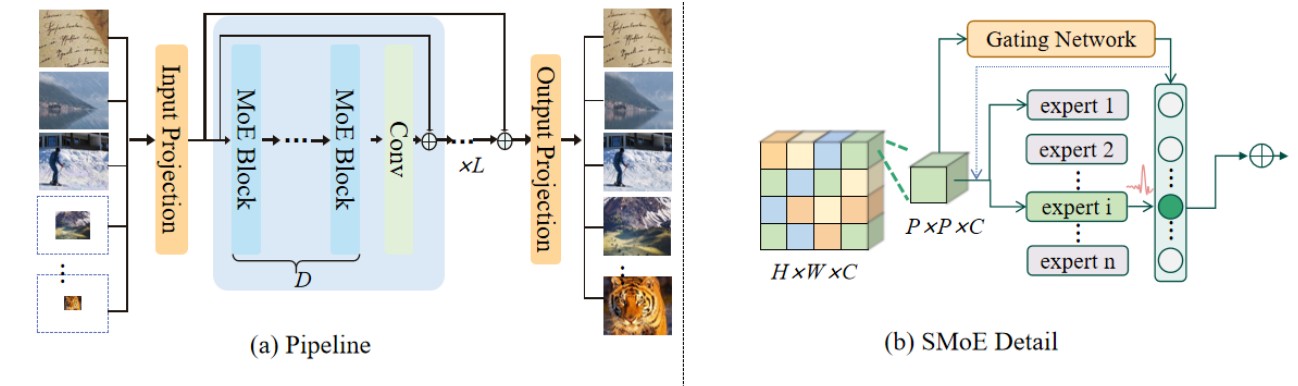


Figure 9. More details about the network. (a) shows the pipeline. (b) introduces the patch-level tokens in SMoE

of different experts for the input x_i . As described in the main text, the $w(x_i)$ is obtained by the gate network in eq. (9). $\mathbf{W}_g \in \mathbb{R}^{n \times C}$ is a trainable parameter, \otimes is the matrix multiplication, $\mathcal{Z}_k(\cdot)$ is the function that sets all values to zeros except the top- k largest values. In this paper, we set $P = 7$ and $k = 1$, which means that for a SMoE Block in eq.(10), only the activated expert $E_j(x_i)$ contributes to the output $y_i = w(x_i)_j E_j(x_i)$. Finally, we merge the output of each input patch, and reshape the flatten embedding back to get the $Y \in \mathbb{R}^{C \times H \times W}$.

C. More Results

C.1. More comparison Under the Same Data Scale.

To further demonstrate the value of the proposed dataset, we compared DAMoE’s performance using ImageNet-50K [21], Laion-50K [41], and our proposed HQ-50K. For ImageNet-50K and Laion-50K, we randomly selected 50,000 images from each dataset. The results are presented in Table 13. As shown, our HQ-50K outperforms the other two datasets across all degradation levels, indicating its su-

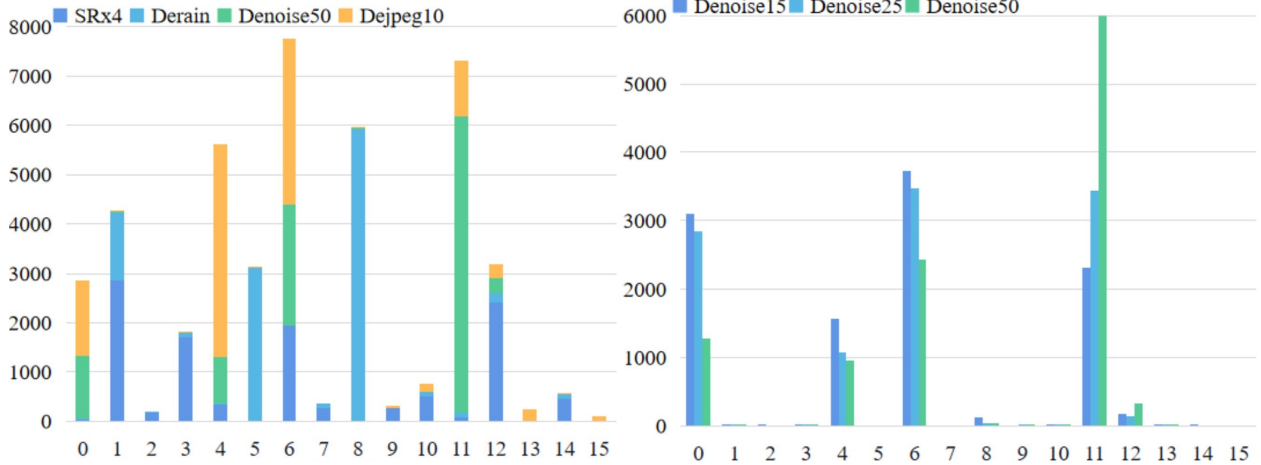


Figure 10. Expert selection pattern of different Task (left) and different degradation levels of the same task (right).

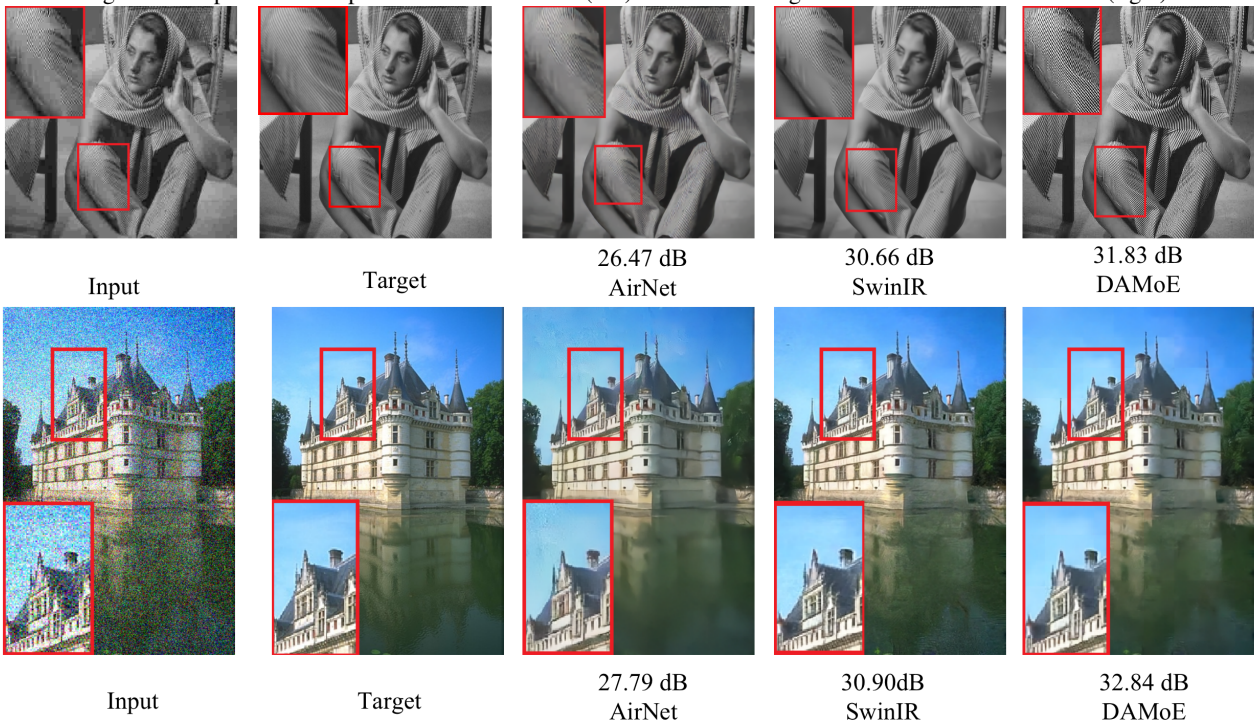


Figure 11. Visual comparisons of different methods on Dejpeg of $q = 10$ on classic5 [14] and on Denoise of $\sigma = 50$ on CBSD68 [36]

perior quality.

C.2. Adaptive Expert Routing of SMoE

We further analyzed the expert selection pattern of SMoE in the MoE block. To this end, we selected the SMoE in the 18th MoE Block, i.e., the SMoE in the middle of the network, as the analysis object, as illustrated in Figure 10. Our findings revealed that for various tasks, the model will make different selections of experts. Moreover, even for the same task with different degradation levels, there are differences in expert routing, albeit not as pronounced as those observed between different tasks. Our results align with the

domain distance of its degraded domain.

C.3. Visual Results

We provide some qualitative comparisons to show the superiority of our DAMoE as the unified restoration model. The Figure 11, 12, 13 show the result of SR, deraining, dejpeg and denoising that all the model are trained on our HQ-50K respectively. For SR, our method suffers from less ringing effects and has sharper texture compared with the others. For deraining, our DAMoE can better remove dense rain streaks. For dejpeg, our results preserve more high-frequency information. And for denoising, DAMoE could



Figure 12. Visual comparisons of different methods on SR of $\times 4$ on Manga109 [17]

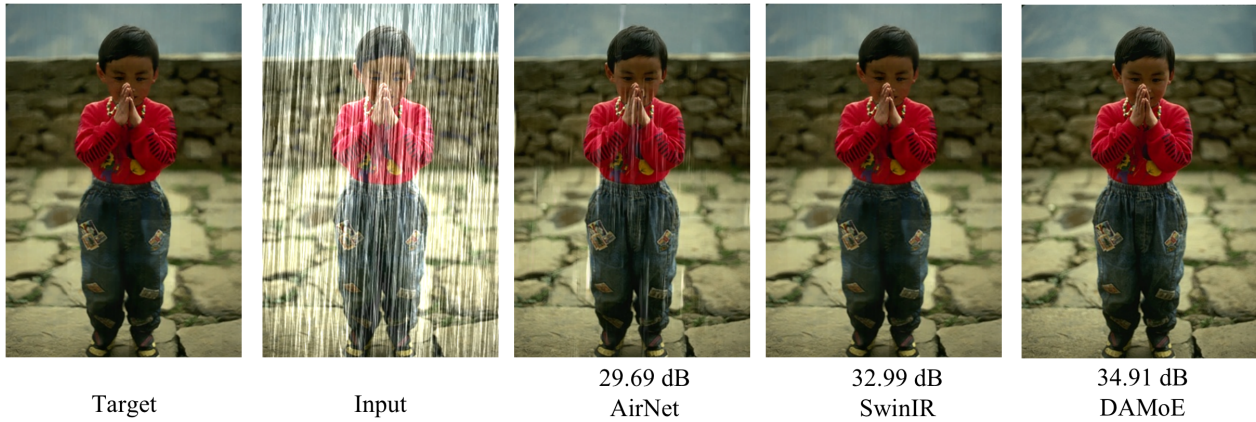


Figure 13. Visual comparisons of different methods on DeRain on Rain100 [52]

Table 13. Comparisons with the multitask results in ALL-in-One DAMoE model trained on ImageNet-50K, Laion-50K and our HQ-50K

Training Set	SR(PSNR-Y) Manga109[17]			DeRain(PSNR-Y) Rain100L[52]	Denoise(PSNR) CBSD68[36]			Dejpeg(PSNR) Classic5[43]			
	x2	x3	x4	-	15	25	50	40	30	20	10
Laion-50K	38.22	33.13	25.24	39.07	34.12	31.47	28.24	33.99	33.18	31.93	29.74
ImageNet-50K	37.27	32.32	25.53	38.59	34.01	31.36	28.10	33.94	33.10	31.83	29.61
HQ-50K	38.51	33.40	26.12	40.22	34.18	31.52	28.28	34.15	33.31	32.03	29.80

restore a cleaner image. This illustrates the effectiveness of integrating the MoE idea for unifying different restoration tasks.